

# Gradient nano-grained graphene as 2D thermal rectifier: A molecular dynamics based machine learning study

Cite as: Appl. Phys. Lett. **121**, 133501 (2022); doi: [10.1063/5.0108746](https://doi.org/10.1063/5.0108746)

Submitted: 10 July 2022 · Accepted: 5 September 2022 ·

Published Online: 26 September 2022



View Online



Export Citation



CrossMark

Ke Xu,<sup>1</sup> Ting Liang,<sup>2</sup> Yuequn Fu,<sup>1</sup> Zhen Wang,<sup>3</sup> Zheyong Fan,<sup>4</sup> Ning Wei,<sup>5</sup> Jianbin Xu,<sup>2</sup> Zhisen Zhang,<sup>1,a)</sup> and Jianyang Wu<sup>1,6,a)</sup>

## AFFILIATIONS

<sup>1</sup>Department of Physics, Research Institute for Biomimetics and Soft Matter, Jiujiang Research Institute and Fujian Provincial Key Laboratory for Soft Functional Materials Research, Xiamen University, Xiamen 361005, People's Republic of China

<sup>2</sup>Department of Electronic Engineering and Materials Science and Technology Research Center, The Chinese University of Hong Kong, Shatin, N.T., Hong Kong 999077, China

<sup>3</sup>Institute of Theoretical Physics, Chinese Academy of Sciences, Beijing 100190, China

<sup>4</sup>College of Physical Science and Technology, Bohai University, Jinzhou 121013, People's Republic of China

<sup>5</sup>Jiangsu Key Laboratory of Advanced Food Manufacturing Equipment and Technology, Jiangnan University, 214122 Wuxi, China

<sup>6</sup>NTNU Nanomechanical Lab, Norwegian University of Science and Technology (NTNU), Trondheim 7491, Norway

<sup>a)</sup>Authors to whom correspondence should be addressed: [zhangzs@xmu.edu.cn](mailto:zhangzs@xmu.edu.cn) and [jianyang@xmu.edu.cn](mailto:jianyang@xmu.edu.cn)

## ABSTRACT

Machine learning has become an excellent tool for scientists and engineers to predict, design, and fabricate next-generation material. Here, we report the thermal conductivity and thermal rectification of gradient-nano-grained graphene (GNNG) by molecular dynamic simulation with machine learning. It is revealed that the thermal conductivity of GNNG is mainly determined by the average grain size, while its thermal rectification factor varies linearly with the gradient of nanograins. Deep neural network-based machine learning models are developed to estimate the thermal transport properties of GNNG using microstructural signatures, such as the location, number, and orientation of 5|7 pairs. The results stress the pivotal roles of 5|7 defects in the planar thermal transports of graphene and indicate that high-performance 2D thermal rectifiers for heat flow control and energy harvesting can be achieved by bio-inspired gradient structure engineering. The findings are expected to supply a theoretical strategy for the design of bio-inspired materials and create a method to predict the potential properties of the material candidates by using machine learning, which can save the abundant expense of developing the material by using the classical method.

Published under an exclusive license by AIP Publishing. <https://doi.org/10.1063/5.0108746>

In nature, there are diverse and excellent structures, such as spirals,<sup>1,2</sup> fractal,<sup>3–5</sup> gradients,<sup>6–8</sup> and so on. With the help of these structures, living organisms survive in various harsh living settings by following natural selection and evolution. For example, climbing plants are arranged in spiral patterns to grow vertically due to the high flexural rigidity against the gravity of spiral structures.<sup>9,10</sup> Byssus threads formed with gradient structures to own spatially varying mechanical properties from soft to stiff for efficiently attaching the mussel to rock.<sup>11</sup> Such structures present in nature maximize their physical and mechanical performances but minimize the cost of materials.

For recent decades, natural structures have been borrowed by mankind to prepare engineering materials with unique and combined properties.<sup>12–14</sup> In the view of mechanics, a variety of artificial gradient

nanostructured metals and alloys have been designed and fabricated to achieve incredible mechanical properties such as high strength-ductility synergy, superior work hardening, outstanding fatigue, and excellent wear- and corrosion-resistance via deformation mechanisms that differ from those in gradient nanostructure-free counterparts.<sup>15,16</sup> In terms of thermal engineering and energy utilization, materials with gradient structures are good candidates for active heat flow control and manipulation.<sup>17,18</sup> For example, graphene-based materials with gradient shape, nanopore defects, and chemical doping show large thermal rectification.<sup>19,20</sup> However, the experimental fabrication of graphene samples with the above gradient structures remains challenging.

In this work, inspired by gradient-structured biosystems [Fig. 1(a)], a gradient structure in 2D graphene is proposed to function

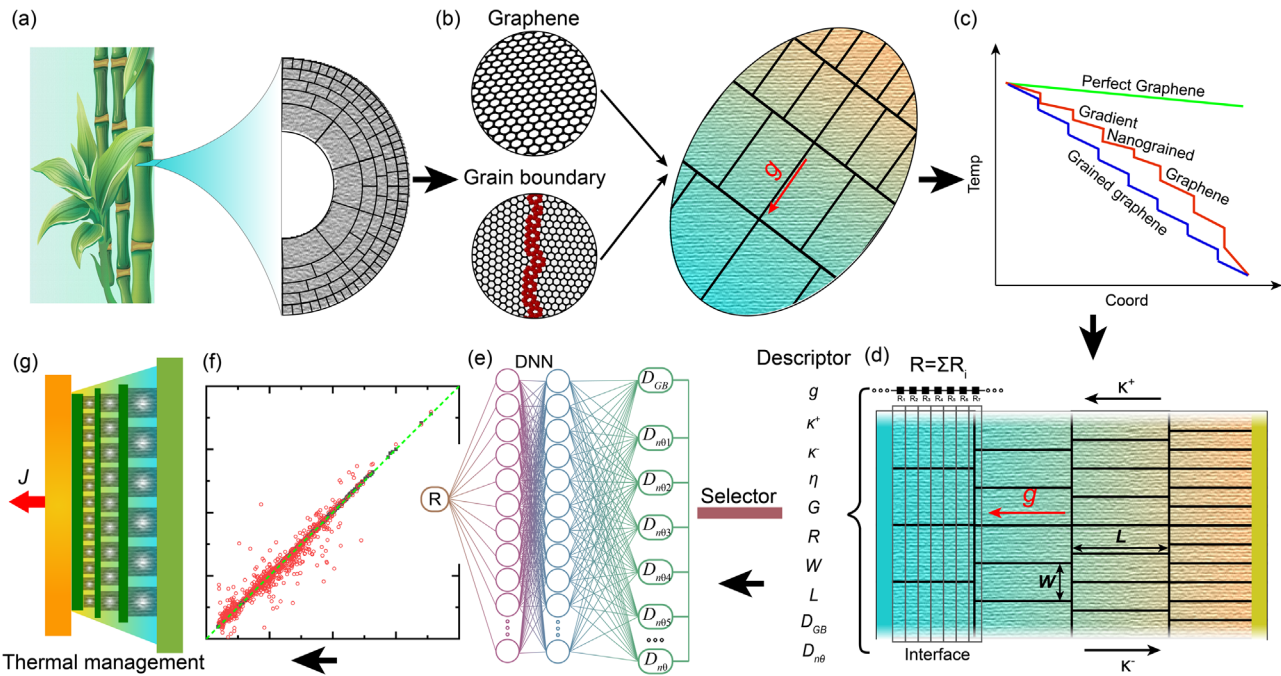


**FIG. 1.** The workflow of this study. (a) Gradient structures in bamboo biosystem. (b) Gradient-nano-grained graphene (GNGG) with spatially varied nanograins, where neighboring nanograins are well stitched by 5/7 defects-dominated grain boundaries (GBs). (c) Schematic diagram of temperature profiles in 2D graphene with different microstructures. (d) Descriptors of GNGG for machine learning study of thermal transport properties. (e) Typical neuron structure for machine learning (ML) study. (f) Prediction of thermal transport properties of GNGG by an as-trained machine learning model. (g) GNGG can be a good candidate as the building block for device systems.

as thermal rectification behavior by spatially adapting the grain size along one in-planar direction. The workflow of this work is shown in Fig. 1. As is known, gradient structures are ubiquitous in biosystems such as bamboo,<sup>6</sup> as seen in Fig. 1(a). Inspired by this, nanocrystalline graphene with gradient grains [Fig. 1(b)] is creatively proposed to achieve desirable heat flow control and manipulation. Neighboring grains are well stitched by grain boundaries (GBs). Because of the presence of defective GBs, there is a non-uniform temperature gradient, and a temperature drop in graphene as a stable heat flux is imposed, as indicated in Fig. 1(c). To obtain physical insights into the thermal transport properties of gradient-nano-grained graphene (GNGG), several descriptors are selected for the machine learning (ML) study [Fig. 1(d)]. A complex multilayer artificial neural network (ANN), also called deep neural network (DNN), is utilized for training [Fig. 1(e)] and developing ML models with the capability of predicting the thermal conductivity [Fig. 1(f)]. It turns out that such GNGG with desirable thermal rectification can be used as ideal building blocks for next-generation device systems [Fig. 1(g)].

In order to generate high-quality structures of polycrystalline graphene close to those obtained by chemical vapor deposition (CVD) methods,<sup>21,22</sup> all the GNGG samples are constructed by the phase field crystal (PFC) model,<sup>23,24</sup> which has been used to build up large, realistic, and locally relaxed microstructures of polycrystalline graphene.<sup>25,26</sup> It should be noted that the PFC-constructed polycrystalline graphene contains energy-favorable GBs dominated by 5/7 pairs, in contrast to Voronoi tessellation method-constructed ones in which diverse energy-unfavorable structural defects such as 4, 8-membered rings and vacancies are richly contained. All the GNGG samples with large dimensionality

(length  $L$  and width  $W$ ) of  $360 \times 100 \text{ nm}^2$  composed of over  $1.35 \times 10^6$  atoms are generated. For convenience, all investigated polycrystalline graphene sheets are marked as  $P_{m-n}^g$ , where  $g$  is the gradient coefficient of grains, while  $m$  and  $n$  are the numbers of grains at the end of samples.

The gradient nanostructures in GNGG are characterized by the spatial gradient in crystalline grain size, defined as the rate in the change of the number of grains per unit length, with expression as  $g = \Delta N / \Delta L$ . Details of GNGG in this work can be referred to Sec. S1. For all samples, the defects of 5/7 pairs are recognized by CountRings.<sup>27</sup> Structural information and simulation details are shown in Sec. S1.

The global and local thermal transport properties of GNGG are investigated. Figures 2(a), 2(c), and 2(f) illustrate heat flux in the structural models. As is illustrated, subjected to stable heat flux from heat source to heat sink, there are smooth changes in temperature in the blocks. However, there are temperature jumps in the blocks in which GBs make large angles to the direction of heat flux. Figure 2(b) compares the global  $\kappa$  of polycrystalline graphene with different  $g$  and average grain sizes. The global  $\kappa$  of polycrystals with  $\bar{d} = 16.5$  and  $31.6 \text{ nm}$  agrees well with the previous results.<sup>28</sup> With increasing  $\bar{d}$ , there is monotonic increase in the global  $\kappa$ . For example, as  $\bar{d}$  varies from 16.5 to  $31.6 \text{ nm}$ , global  $\kappa$  varies from  $311.7$  to  $490.2 \text{ W m}^{-1} \text{ K}^{-1}$  by around 57.3%. However, there is a negligible difference in the global  $\kappa$  between  $P_{m-n}^g$  and  $P_{m-n}^0$  models with similar  $\bar{d}$ . This indicates that  $g$  does not play an important role in the global  $\kappa$  of polycrystalline graphene. Local thermal transport properties are also examined, as shown in Figs. 2(d) and 2(e). As indicated, with the density decreasing of grains, there is a linear increase in the  $1/\kappa$ . By this linear relation,  $\kappa$  of grain with infinite  $L$  and  $W = 30 \text{ nm}$  is extrapolated to be around

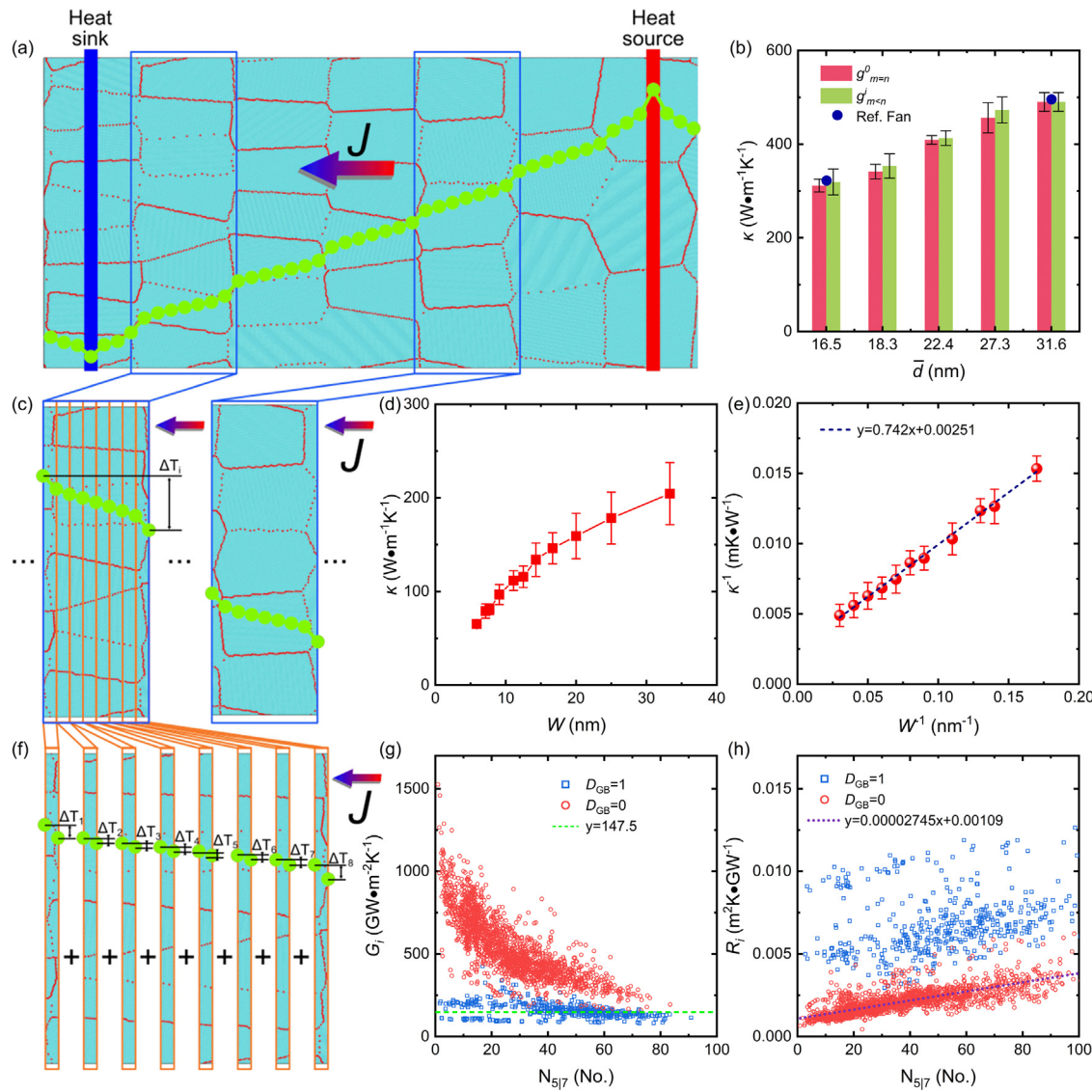


**FIG. 2.** (a) Schematic diagram of gradient-nano-grained graphene (GNNG) subjected to stable heat flow. The blue and red regions are the heat sink and heat source locations, respectively. The green dots crossing the structure indicate the variation of temperature. (b) Global  $\kappa$  of GNNG as a function of  $\bar{d}$ , where blue circle points are from the previous study.<sup>28</sup> (c) and (f) Schematic diagrams of thermal transport properties of local GNNG for the next machine learning treatment. (d) and (e) Variation in the  $\kappa$  and  $\kappa^{-1}$  with width ( $W$ ). (g) and (h)  $G_i$  and  $R_i$  as a function of the number of 5|7 defect ( $N_{5|7}$ ) in GNNG, where the blue and red dots represent the grain boundaries (GBs) that make large ( $\geq 45^\circ$ ) and small ( $A45^\circ$ ) angles to the direction of heat flux, respectively.

397 W/m K, in agreement with previous results.<sup>29,30</sup> Furthermore, the relationship between local  $G_i$  and the number of 5|7 dislocation ( $N_{5|7}$ ) at GBs is studied, as shown in Fig. 2(g). Here, 5|7 dislocation at GB that makes the average angle of  $<45^\circ/\geq 45^\circ$  to heat flux direction is marked as  $D_{GB} = 0/1$ . When  $D_{GB} = 1$ , local  $G$  fluctuates at a constant value around 147.5 GW m<sup>-2</sup> K<sup>-1</sup>, indicating that local  $G_i$  is negatively influenced by  $N_{5|7}$  at GBs. As  $D_{GB} = 0$ , however, local  $G$  is monotonically reduced with increasing  $N_{5|7}$ , and the reduction in  $G$  becomes insignificant. As shown in Fig. 2(h), there is a linear relationship between  $R_i$  and  $N_{5|7}$ . Based on this linear relationship, 5|7 dislocation-free structure shows  $R_i = 0.001\ 09\text{ m}^2\text{ K}\text{ GW}^{-1}$ .

As illustrated by Fig. 3(a), the gradient grain size and gradient density of 5|7 defect along one planar direction, heat current preferentially transported toward the region with large grain or less 5|7 defect. This indicates that GNNG is a good candidate for a realistic thermal rectifier. Figure 3(b) compares the variation in the temperature with the position of the graphene with defect-free,  $g = 0$  and 0.033. As a stable heat flux is imposed, there are distinct variations of local temperature between them. Such differences can be mainly attributed to their distinct distribution and density of 5|7 defects. Figure 3(c) shows the global  $\kappa$  and  $N_{5|7}$  of GNNG samples as a function of  $g$ . With the increase in  $g$ ,  $N_{5|7}$  of GNNG samples is monotonically increased, while

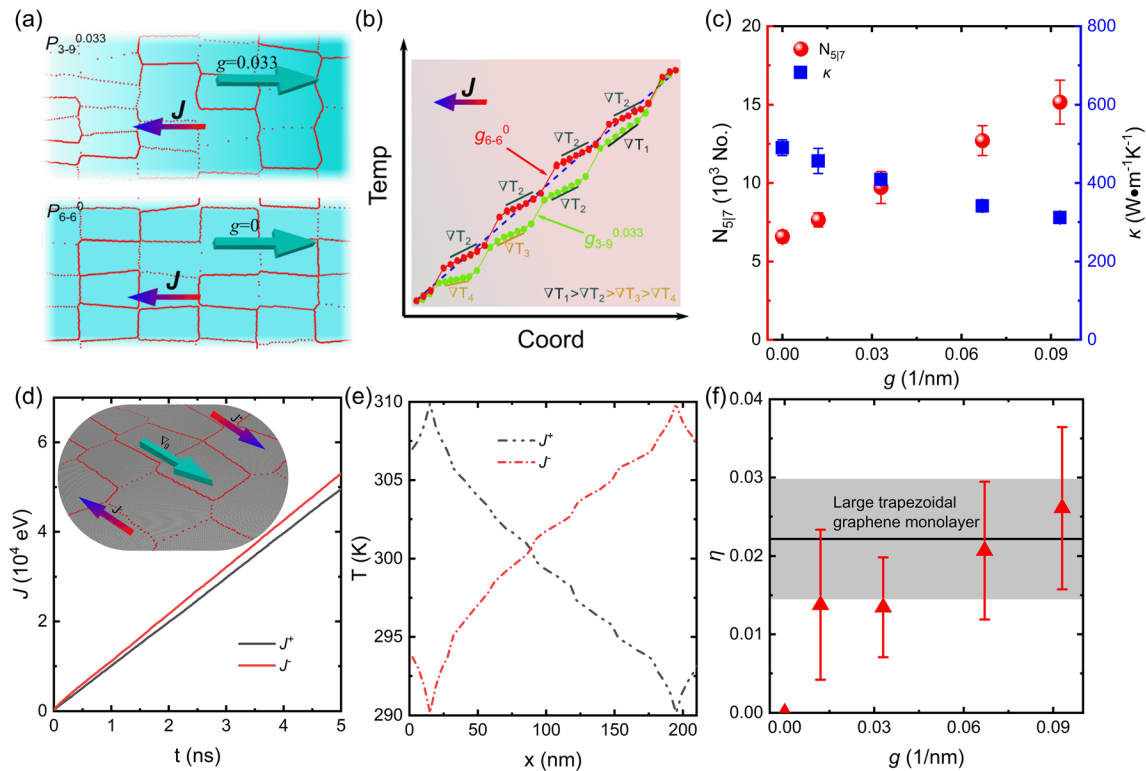


**FIG. 3.** (a) Schematic of heat flow on GNGG with  $g = 0$  and  $0.033$ . (b) Typical temperature profiles of GNGG with  $g = 0$  and  $0.033$  as well as perfect graphene. (c) The number of  $5|7$  defect and global  $\kappa$  of GNGG as a function of gradient coefficient  $g$ . (d) Typical heat flow transfer as a function of time. Inset is the local structure of GNGG, where the arrows represent the heat flow and gradient nanograins. (e) Comparison of typical temperature profiles of GNGG as heat flow is reversely applied. (f) The ratio of thermal rectification as a function of  $g$  in GNGG. The black region indicates the thermal rectification factor of the trapezoidal graphene monolayer.<sup>30</sup>

the global  $\kappa$  is reduced. Figure 3(d) presents the heat fluxes ( $J^+$  and  $J^-$ ) as a function of time, where  $J^+$  and  $J^-$  are defined by that the applied heat current is from small-to-large and large-to-small grains in GNGG, respectively. When identical temperatures are controlled at both regions of hot source and hot sink,  $J^+ < J^-$ , resulting from the gradient nanograins in GNGG. The global  $\kappa$  of polycrystalline graphene under  $J^+$  and  $J^-$  with different  $\bar{d}$  is shown in Fig. S4(a). As  $J^+$  and  $J^-$  imposed, their temperature profiles in the GNGG samples are displayed in Fig. 3(e). The temperatures are nonlinearly changed from hot source to hot sink due to the presence of  $5|7$  defects. Based on the temperature profiles, both  $\kappa^+$  and  $\kappa^-$  can be determined. As a result, the thermal rectification coefficient  $\eta$  of GNGG is calculated by  $\eta = (\kappa^+ - \kappa^-)/\kappa^+$ . Figures 3(f) and S2(b) present the variation in the  $\eta$  and  $N_{5|7}$  with  $g$ . In-plane  $\eta$  of GNGG is enhanced with increasing  $g$ , and the number of  $5|7$  defects is also enhanced with increasing  $g$ . When  $g = 0.093$  and  $\bar{d} = 16.5$  nm, in-plane  $\eta$  of GNGG achieves 2.61%. As shown in Fig. 3(f), in-plane  $\eta$  is larger than the large trapezoidal graphene monolayer. Such  $\eta$  is similar to that of off-plane multilayer graphene with gradient hydrogenation.<sup>19</sup> Moreover, in-plane  $\eta$  in GNGG with a given  $g$  can be effectively tuned by  $\bar{d}$ . As shown in Fig. S4(c), the in-plane  $\eta$  in GNGG is decreased with  $\bar{d}$ . In a nutshell, in-plane  $\eta$  in GNGG can be well controlled via nano-grained engineering.

To summarize, the thermal transport properties such as  $G$ ,  $R$ ,  $\kappa^+$ ,  $\kappa^-$ , and  $\eta$  of GNGG structures are greatly dictated by the global

structural characteristics such as  $g$ ,  $W$ , and  $L$ . For perfect graphene, it shows isotropic  $\kappa$ ,<sup>31,32</sup> whereas for defective graphene-like GNGG, the thermal transport properties are highly influenced by the nanostructure defects. As indicated in Figs. 2(g) and 2(h), the location, number, and orientation of  $5|7$  defects are important internal factors affecting the thermal transport properties of GNGG. Therefore, two creative descriptors, including the interface location ( $D_{GB}$ ) and the number and orientation of  $5|7$  defect ( $D_{n\theta}$ ), are selected in the following ML study. All GNGG models with  $L = 360$  nm are divided into 12 blocks, and each block is split into seven regions, as schematized in Fig. 4(a). As a result, there are 12 and 68 regions of  $D_{GB} = 1$  and 0, respectively, where four regions corresponding to the heat source and heat sink areas are removed. For example, as shown in Fig. 4(a), regions of  $S_1$  and  $S_8$  are marked as  $D_{GB} = 1$ , while others are marked as  $D_{GB} = 0$ . Therefore, the location of  $5|7$  defects is defined. In addition, to characterize the number and orientation distribution of  $5|7$  defects, angle distribution function descriptor with a mathematical expression  $D_{n\theta} = \sum N_{5|7}(\theta)\Delta\theta$  is defined. To describe the orientation of  $5|7$  defect, an angle between the line passed the top and bottom carbon atoms of  $5|7$  pairs, and the horizontal line is defined as shown in the inset of Fig. 4(b). To plot the orientational profile of  $5|7$  defect, a subdivision of  $\Delta\theta$  is used to count  $N_{5|7}$ . Figures 4(b) and 4(c) show the orientational profiles of  $5|7$  defect and  $N_{5|7}$  in regions of  $S_1$  and  $S_2$  as  $\Delta\theta = 2^\circ$ , respectively. Based on the MD results, a total of 6795 data

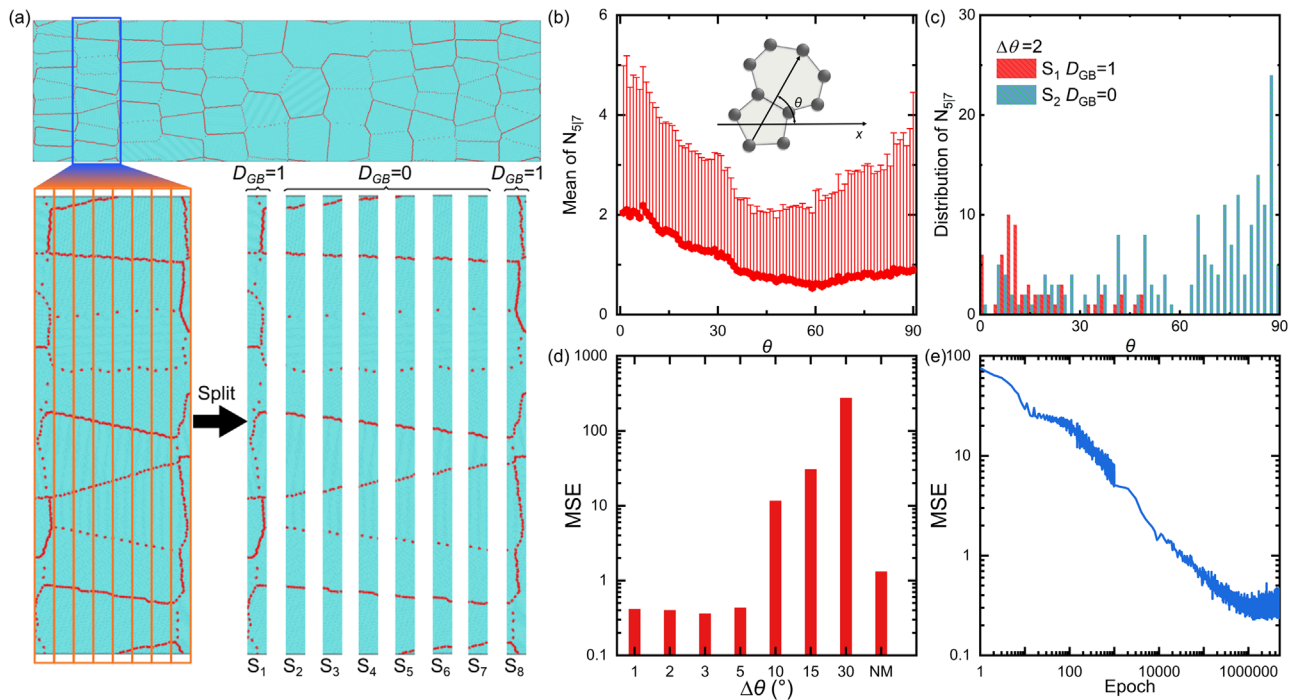


**FIG. 4.** (a) Global and local structures of GNGG in which microstructural information such as the location of GBs is selected as features for the machine learning (ML) study. The GBs that are vertically/horizontally oriented are defined as  $D_{GB} = 0$  and 1. (b) The number of 5|7 pair as a function of orientational angle  $\theta$ , where the inset defines the orientational angle of 5|7 defect. (c) The distribution of  $N_{5|7}$  at regions of  $D_{GB} = 0$  and 1 as a function of  $\theta$ . (d) MSE as a function of  $\Delta\theta$  and no- $D_{GB}$ . (e) Variation in the MSE with Epoch.

points were collected, and each data point has dimensions of  $90^\circ/\Delta\theta + 1$ . Figure 4(d) shows the mean squared error (MSE) as a function of  $\Delta\theta$ . As is revealed, when  $\Delta\theta \leq 5^\circ$ , small values of MSE are achieved. Figure 4(e) presents the variation in the value of MSE with Epoch. It is found that there is a reduction trend in the value of MSE with increasing Epoch. As is indicated, a number of 1 000 000 for Epoch can reach a reasonable value of MSE.

Figure 5 compares the ANN-based ML results by using different variables of  $\Delta\theta = 5^\circ$ ,  $2^\circ$ , and  $1^\circ$ , and four neuron compositions. To find the right combination of the number of neurons and hidden layers, the four neuron compositions include one layer with 512 neurons (ANN-M1), two layers with 512 + 256 neurons (ANN-M2), three layers with 1024 + 512 + 256 neurons (ANN-M3), and six layers with 1024 + 1024 + 512 + 512 + 256 + 256 neurons (ANN-M4), as illustrated in the inset of Figs. 5(a)-5(d), respectively. Additionally, the ANN-based ML results by the single-layer neural network are collected in Sec. S3 as a part of supplementary material for more details on molecular dynamics (MD) calculations and code of machine learning model predictions. With the same number of neurons, a better model can be obtained by increasing the number of neuron network layers. There is an effect of neuron composition on the ML results. As is expected, a complex neuron structure ANN-M4 achieves the best performance in predicting the thermal transport properties such as  $G$  and  $R$ . Furthermore, as is revealed in Figs. 5(e)-5(i),  $\Delta\theta$  also influences the ML results by ANN-M4. As  $\Delta\theta = 1^\circ$ , ANN-M4 exhibits the best performance in predicting the thermal transport properties of GNGG. By comparing ANN-M4 with  $\Delta\theta = 1^\circ$  achieves the best performance

in predicting the thermal transport properties of GNGG, with an MSE value of 1.2. This demonstrates that our developed ANN-M4 ML model is capable of predicting the thermal transport properties of polycrystalline graphene by extracting the structural information of GBs, the number and orientation of 5|7 defect. Such a ANN-based ML framework can be utilized for the prediction of thermal transport properties of other 2D materials in which GBs and dislocation defects are richly contained. The ML dataset and one of the trained ANN models are available as described in Sec. S4 of the supplementary material. Note that, for all ANN ML models, particularly for the DNN model, the selection of training parameters is time-consuming. Furthermore, many efforts should be made to check data integrity, ensuring that the most important features are included.

The ANN-based ML models uncover the relationship between the microstructural information of the GB-contained interface and the thermal transport properties of GNGG structures. Analysis shows that the ML results rely not only on  $g$  but also on the distribution of 5|7 defect at the GB-contained interfaces, for example,  $R_i = \text{ANN}(D_{GB}^i, D_{5|7}^i)$ . By Ohm's law ( $R = \sum_i R_i$ ), the  $\kappa$  of GNGG is expressed as

$$\kappa = \frac{L}{R} = \frac{L}{\sum_i R_i} = \frac{L}{\sum_i \text{ANN}(D_{GB}^i, D_{5|7}^i)}.$$

As a result, the  $\kappa$  of nanocrystalline graphene can be estimated from hidden microstructural information. As is known, however, realistic CVD-grown polycrystalline graphene is usually in micro/millimeter size, in which the crystalline grains can be hundreds of nanometer

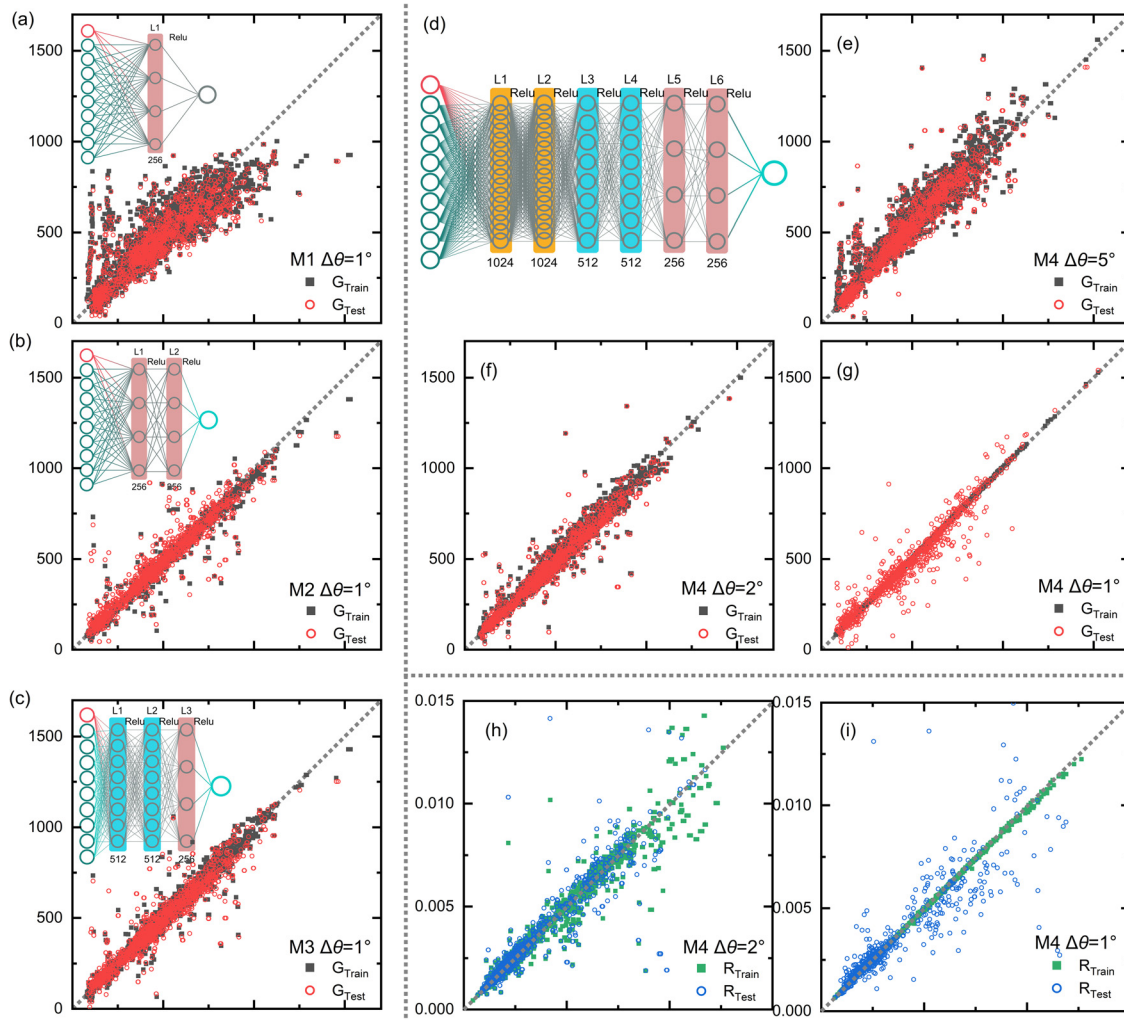


**FIG. 5.** (a)–(c) show the training and testing results of  $G$  of GNGG by three different neuron structures, marked as ANN-M1, ANN-M2, and ANN-M3, respectively. Inset indicates the neuron structures. (d) Schematic diagram of the complex six-layered neuron structure with  $1024 + 1024 + 512 + 512 + 256 + 256$  neurons, marked as ANN-M4. (e)–(g) show the training and testing results of  $G$  of GNGG by ANN-M4 with  $\Delta\theta = 5^\circ$ ,  $2^\circ$ , and  $1^\circ$ , respectively. (h) and (i) show the training and testing results of  $R$  of GNGG by ANN-M4 with  $\Delta\theta = 2^\circ$  and  $1^\circ$ , respectively.

size. Although multiscale modeling such as coupled molecular mechanics (MM)/MD methods with finite element method (FEM) was proposed to investigate the properties of graphene-based materials at different size scale,<sup>33–35</sup> our proposed ML-based models could also be utilized to achieve the prediction for the properties of large-sized polycrystalline graphene.

In summary, polycrystalline graphene with spatially varying nanograins (GNGG) is originally proposed, and their thermal transport properties are investigated via a combination of non-equilibrium MD simulations and ANN-based ML. The  $\kappa$  of GNGG is mainly controlled by  $\bar{d}$ , in agreement with that of conventional polycrystalline graphene. For example, GNGG and conventional polycrystalline graphene that own similar  $\bar{d}$  show similar  $\kappa$ . Especially, GNGG shows thermal rectification behavior due to the presence of spatially varying nanograins, and the  $\eta$  of GNGG is linearly varied with  $g$ . Based on

using structural information such as the location, number, and orientation of 5/7 defects, ANN-based ML models with different neuron structures are developed to predict the thermal transport properties of GNGG. Different ML setting parameters and  $\Delta\theta$  are discussed in the ML study. The best performance of the as-developed ANN-based ML model can predict the thermal transport properties of GNGG, with an MSE value of 1.2. This work demonstrates the capability of our developed ANN-based ML models in uncovering the relationship between microstructure-thermal properties in GNGGs, providing a strategy for material design with desirable properties using data-driven approaches.

See the [supplementary material](#) for more details on molecular dynamics calculations and code of machine learning model predictions.

We thank Chaoyun You for his helpful comments. This work was financially supported by the National Natural Science Foundation of China (Grant Nos. 12172314, 11772278, and 11904300), the Jiangxi Provincial Outstanding Young Talents Program (Grant No. 20192BCBL23029), the Research Grants Council of Hong Kong (Grant No. AoE/P-701/20), and the Fundamental Research Funds for the Central Universities (Xiamen University: Grant Nos. 20720210025 and 20720220023). Shaorong Fang and Tianfu Wu from the Information and Network Center of Xiamen University are acknowledged for their help with GPU computing.

## AUTHOR DECLARATIONS

### Conflict of Interest

The authors have no conflicts to disclose.

### Author Contributions

**Ke Xu:** Conceptualization (lead); Data curation (lead); Formal analysis (lead); Writing – original draft (equal). **Ting Liang:** Conceptualization (equal); Data curation (equal); Formal analysis (equal). **Yuequn Fu:** Investigation (equal); Methodology (equal). **Zhen Wang:** Investigation (equal); Methodology (equal). **Zheyong Fan:** Methodology (equal); Project administration (equal); Resources (equal). **Ning Wei:** Supervision (equal); Visualization (equal); Writing – review & editing (equal). **Jianbin Xu:** Writing – review & editing (equal). **Zhisen Zhang:** Writing – review & editing (equal). **Jianyang Wu:** Methodology (equal); Writing – original draft (equal); Writing – review & editing (equal).

## DATA AVAILABILITY

The data that support the findings of this study are available from the corresponding authors upon reasonable request.

## REFERENCES

- <sup>1</sup>W. Munk, L. Armi, K. Fischer, and F. Zachariasen, *Proc. R. Soc. London, Ser. A* **456**(1997), 1217 (2000).
- <sup>2</sup>A. S. Tatham and P. R. Shewry, *Trends Biochem. Sci.* **25**(11), 567 (2000).
- <sup>3</sup>A. E. Carmo-Silva, A. Francisco, S. J. Powers, A. J. Keys, L. Ascensão, M. A. J. Parry, and M. C. Arrabaça, *Am. J. Bot.* **96**(7), 1222 (2009).
- <sup>4</sup>E. R. Weibel, *Am. J. Physiol.: Lung Cell Mol. Physiol.* **261**(6), L361 (1991).
- <sup>5</sup>R. V. Solé, S. A. Levin, J. H. Brown, V. K. Gupta, B.-L. Li, B. T. Milne, C. Restrepo, and G. B. West, *Philos. Trans. R. Soc., B* **357**(1421), 619 (2002).
- <sup>6</sup>S. Amada, T. Munekata, Y. Nagase, Y. Ichikawa, A. Kirigai, and Y. Zhifei, *J. Compos. Mater.* **30**(7), 800 (1996).
- <sup>7</sup>L. Sardelli, D. P. Pacheco, L. Zorzetto, C. Rinoldi, W. Święszkowski, and P. Petrini, *J. Funct. Biomater.* **17**(1), 228080001982902 (2019).
- <sup>8</sup>Y. Liu, A. Li, and S. Chen, *J. Phys.: Conf. Ser.* **1176**, 022019 (2019).
- <sup>9</sup>S. Isnard, A. R. Cobb, N. M. Holbrook, M. Zwieniecki, and J. Dumais, *Proc. R. Soc. B* **276**(1667), 2643 (2009).
- <sup>10</sup>J. Wu, Q. Shi, Z. Zhang, H.-H. Wu, C. Wang, F. Ning, S. Xiao, J. He, and Z. Zhang, *Nanoscale* **10**(33), 15641 (2018).
- <sup>11</sup>K. U. Claussen, T. Scheibel, H.-W. Schmidt, and R. Giesa, *Macromol. Mater. Eng.* **297**(10), 938 (2012).
- <sup>12</sup>Y. Lin, J. Pan, H. F. Zhou, H. J. Gao, and Y. Li, *Acta Mater.* **153**, 279 (2018).
- <sup>13</sup>J. I. Ziegler and R. F. Haglund, *Nano Lett.* **10**(8), 3013 (2010).
- <sup>14</sup>Z. Qin, B. G. Compton, J. A. Lewis, and M. J. Buehler, *Nat. Commun.* **6**(1), 7038 (2015).
- <sup>15</sup>Z. Cheng, H. Zhou, Q. Lu, H. Gao, and L. Lu, *Science* **362**(6414), eaau1925 (2018).
- <sup>16</sup>X. Li, L. Lu, J. Li, X. Zhang, and H. Gao, *Nat. Rev. Mater.* **5**(9), 706 (2020).
- <sup>17</sup>R. Gao, Z. Fan, and S. Liu, *J. Energy Storage* **48**, 104014 (2022).
- <sup>18</sup>S. Feng, Y. Yan, H. L. Li Zhang, and S. Yang, *Appl. Therm. Eng.* **182**, 116132 (2021).
- <sup>19</sup>A. Wei, S. Lahkar, X. Li, S. Li, and H. Ye, *ACS Appl. Mater. Interfaces* **11**(48), 45180 (2019).
- <sup>20</sup>H. Wang, S. Hu, K. Takahashi, X. Zhang, H. Takamatsu, and J. Chen, *Nat. Commun.* **8**(1), 15843 (2017).
- <sup>21</sup>P. Y. Huang, C. S. Ruiz-Vargas, A. M. van der Zande, W. S. Whitney, M. P. Levendorf, J. W. Kevek, S. Garg, J. S. Alden, C. J. Hustedt, Y. Zhu, J. Park, P. L. McEuen, and D. A. Muller, *Nature* **469**(7330), 389 (2011).
- <sup>22</sup>K. Kim, Z. Lee, W. Regan, C. Kisielowski, M. F. Crommie, and A. Zettl, *ACS Nano* **5**(3), 2142 (2011).
- <sup>23</sup>K. R. Elder and M. Grant, *Phys. Rev. E* **70**(5), 051605 (2004).
- <sup>24</sup>K. R. Elder, M. Katakowski, M. Haataja, and M. Grant, *Phys. Rev. Lett.* **88**(24), 245701 (2002).
- <sup>25</sup>P. Hirvonen, M. M. Ervasti, Z. Fan, M. Jalalvand, M. Seymour, S. M. Vaez Allaei, N. Provatas, A. Harju, K. R. Elder, and T. Ala-Nissila, *Phys. Rev. B* **94**(3), 035414 (2016).
- <sup>26</sup>D. Taha, S. Mkhonta, K. Elder, and Z.-F. Huang, *Phys. Rev. Lett.* **118**(25), 255501 (2017).
- <sup>27</sup>M. Matsumoto, A. Baba, and I. Ohmine, *J. Chem. Phys.* **127**(13), 134504 (2007).
- <sup>28</sup>Z. Fan, P. Hirvonen, L. F. C. Pereira, M. M. Ervasti, K. R. Elder, D. Donadio, A. Harju, and T. Ala-Nissila, *Nano Lett.* **17**(10), 5919 (2017).
- <sup>29</sup>X. Gu, Z. Fan, H. Bao, and C. Y. Zhao, *Phys. Rev. B* **100**(6), 064306 (2019).
- <sup>30</sup>Z. Li, S. Xiong, C. Sievers, Y. Hu, Z. Fan, N. Wei, H. Bao, S. Chen, D. Donadio, and T. Ala-Nissila, *J. Chem. Phys.* **151**(23), 234105 (2019).
- <sup>31</sup>G. Fugallo, A. Cepellotti, L. Paulatto, M. Lazzeri, N. Marzari, and F. Mauri, *Nano Lett.* **14**(11), 6109 (2014).
- <sup>32</sup>Z. Fan, L. F. C. Pereira, H.-Q. Wang, J.-C. Zheng, D. Donadio, and A. Harju, *Phys. Rev. B* **92**(9), 094301 (2015).
- <sup>33</sup>B. Mortazavi, O. Benzerara, H. Meyer, J. Bardon, and S. Ahzi, *Carbon* **60**, 356 (2013).
- <sup>34</sup>M. H. Ulz, *J. Mech. Phys. Solids* **74**, 1–18 (2015).
- <sup>35</sup>Y. Chandra, S. Adhikari, E. I. Saavedra Flores, and L. Figiel, *Mater. Sci. Eng.: R* **140**, 100544 (2020).